

## Research Article

# Influence of Splitter Blades on the Flow Field of a Centrifugal Pump: Test-Analysis Comparison

G. Kergourlay, M. Younsi, F. Bakir, and R. Rey

*LEMFI, Ecole Nationale Supérieure d'Arts et Métiers, 75013 Paris, France*

Received 31 March 2006; Revised 21 November 2006; Accepted 21 November 2006

Recommended by Chunill Hah

This work aims at studying the influence of adding splitter blades on the performance of a hydraulic centrifugal pump. The studied machine is an ENSIVAL-MORET MP 250.200.400 pump (diameter = 408 mm, 5 blades, specific speed = 32), whose impeller is designed with and without splitter blades. Velocity and pressure fields are computed using unsteady Reynolds-averaged Navier-Stokes (URANS) approach at different flow rates. The sliding mesh method is used to model the rotor zone motion in order to simulate the impeller-volute casing interaction. The flow morphology analysis shows that, when adding splitter blades to the impeller, the impeller periphery velocities and pressures become more homogeneous. An evaluation of the static pressure values all around the impeller is performed and their integration leads to the radial thrust. Global and local experimental validations are carried out at the rotating speed of 900 rpm, for both the original and the splitter blade impellers. The head is evaluated at various flow rates: 50%, 80%, 100%, and 120% of the flow rate at the best efficiency point (BEP). The pressure fluctuations are measured at four locations at the BEP using dynamic pressure sensors. The experimental results match the numerical predictions, so that the effect of adding splitter blades on the pump is acknowledged. Adding splitters has a positive effect on the pressure fluctuations which decrease at the canal duct.

Copyright © 2007 G. Kergourlay et al. This is an open access article distributed under the Creative Commons Attribution License, which permits unrestricted use, distribution, and reproduction in any medium, provided the original work is properly cited.

## 1. INTRODUCTION

The design of radial and mixed flow centrifugal pumps still remains very empirical. The impeller and volute geometry is usually chosen according to several optimization criteria such as uniform flow, low machine footprint, stable characteristic curves, and performance improvement (efficiency, NPSH, noise, pressure fluctuations, etc.). During the last few years, the design and performance analyses of turbomachinery have experienced great progress due to the joint evolution of computer power and the accuracy of numerical methods.

Several authors have suggested to combine different computational tools in order to design and analyze turbomachineries [1–5]. Despite the great progress of the turbomachinery design and performance analysis produced by power computer and numerical methods accuracy, the effect of splitter blades on pump performance has not been totally understood.

In the current design of centrifugal compressors and high performance rocket turbo pumps, it is usually recognized that higher mass flow can be passed through the impeller by reducing the blade blockage in the inlet region by

means of splitters [6]. In addition, hydraulic performances are improved, pressure fluctuations are reduced, and operating range is extended. Chiang and Fleeter [7] proposed to use splitter blades as a passive flutter (an undesirable oscillation) control technique. They developed a mathematical model for incompressible flow to predict the aero-dynamical stability of a split-rotor. They used this model to demonstrate that incorporating splitters into unstable rotor configurations results in a stable split-rotor configuration. Comparisons of the non-splitter and splitter versions of a compressor in transonic regime have been realized in [8]. Measurements show that the amplitude of the axial flow distortion increases while the blade-to-blade heterogeneities decrease. In the case of subsonic pumps, the available literature does not mention any complete study of the splitter blade effect.

This work aims at studying the splitter blades effect on the performance of a centrifugal pump through both numerical simulation and experimental results. The original studied machine is an ENSIVAL-MORET MP 250.200.400 pump (diameter = 408 mm, 5 blades, specific speed = 32) whose impeller is designed in two versions: the original and the splitter model. Velocity and pressure fields are computed

TABLE 1: Geometrical characteristic values.

Impeller	
$R_0$	115 mm
$R_1$	75 mm
$b_1$	85.9 mm
$\beta_1$	70°
$\theta_1$	37°
$R_2$	204.2 mm
$b_2$	42 mm
$\beta_2$	63°
$\theta_2$	90°
$N_a$	5
$e$	8 mm
Volute	
$R_3$	218 mm
$b_3$	50 mm
$\Phi_{\text{outlet}}$	200 mm

using unsteady Reynolds-averaged Navier-Stokes (URANS) approach at different flow rates at the rotational speed of 900 rpm.

Section 2 presents the two different pumps geometry. Section 3 gives results on the impeller-volute 3D-flow simulation for the two configurations. Section 4 describes the experimental setup to measure the 3D unsteady pressure components, and their comparison with the computed data at the best efficiency point (BEP).

## 2. DESCRIPTION OF THE PUMP CONFIGURATIONS

### 2.1. Pumps geometry

The original impeller has a specific speed of 32. The main pump (impeller + volute) parameters are presented in Table 1.

The pump impeller was modified adding splitter blades 50% shorter than originals and keeping the same discharge blade angle  $\beta_2$ . The circumferential position of the splitter blades has been chosen in the middle of the blade-to-blade space (mid-channel splitter blades). The original and splitted impeller photographs are presented in Figure 1, the complete pump (impeller + volute casing) is shown in Figure 2.

### 2.2. Experimental facility

The test installation at the LEMFI is composed of two independent but interconnected loops: one for centrifugal pumps, another for axial pumps.

The centrifugal pump loops can be reduced to the diagram of Figure 3. It has the following main parts.

- (i) Two storage tanks with a capacity of 4 m<sup>3</sup>, connected by a pipe of 350 mm diameter. They can be filled and emptied with the help of two electro valves.



FIGURE 1: Original (left) and splitted (right) impellers.



FIGURE 2: Pump with original impeller.

- (ii) A liquid ring vacuum pump is used to control the pressure at the free surface inside the storage tanks.
- (iii) A motorized valve serves to control the pump flow rate in a precise manner.
- (iv) A 45 kW electric motor controlled by variation of input frequency.
- (v) A central control and measurement console.
- (vi) The centrifugal pump furnished with transparent shroud.
- (vii) Electromagnetic flowmeter KROHNE, placed at the pump output.
- (viii) Metallic manometers backed up by piezoresistive pressure sensor.
- (ix) Five piezoelectric pressure sensors, KISTLER brand, 601A type.

## 3. 3D-FLOW SIMULATION

The two pump designs are studied similarly. The computer aided design (CAD) and the mesh generation are first performed, along with the choice of simulations parameters and boundary conditions (Section 3.1). Then the computational flow dynamics (CFD) analysis leading to the global characteristics (Section 3.2) is performed using Fluent 6.2

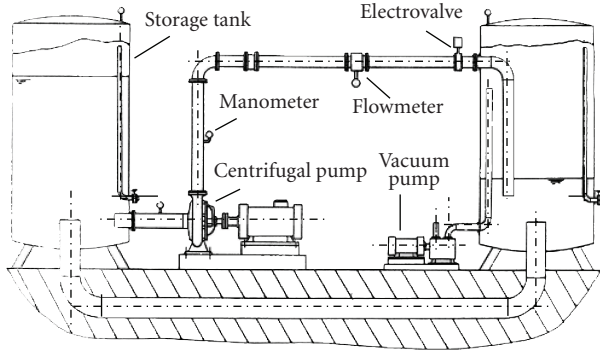


FIGURE 3: A scheme of the LEMFI pump test-ring.

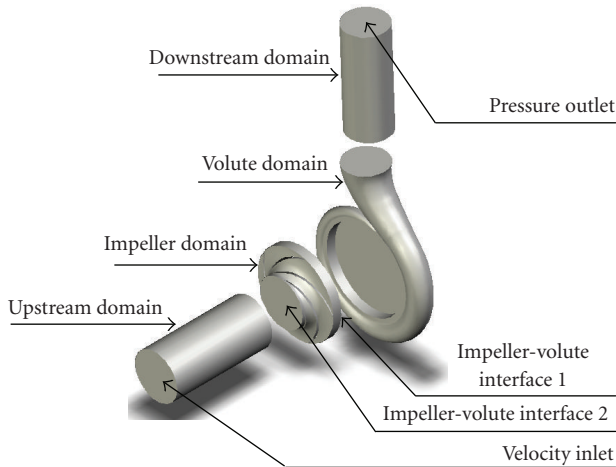


FIGURE 4: Flow and boundary condition domains.

software [9]. The flow morphology analysis (Sections 3.3.1 and 3.3.2) is detailed. Finally, the integration of the predicted static pressure around the impeller leads to the radial thrust (Section 3.4).

### 3.1. Geometry modeling and mesh generation: simulation parameters and boundary conditions

The computational domain is divided into two zones, a rotational zone including the impeller and stationary zones elsewhere. For numerical stability reasons, and to minimize edge effects, this computational domain is extended upstream and downstream. The CAD of this configuration, as well as the boundary conditions, are shown in Figure 4.

The resulting geometry is used to build a hybrid mesh. A grid refinement is studied and adapted to the flow morphology; Figure 5 shows the influence of the cell number on the difference of static pressure between inlet and outlet. According to this figure, the grid (about 1.5 million cells) is considered to be sufficiently enough to ensure mesh independence.

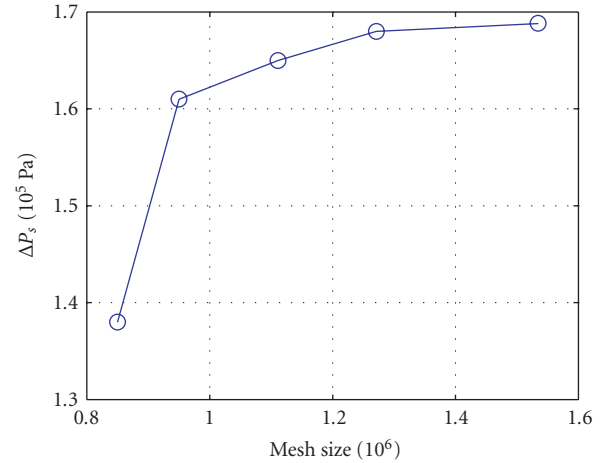


FIGURE 5: Influence of the grid size on the solution—nonsplitted pump at BEP.

Figure 6 shows the volute, impeller, and the surface blade meshes. Table 2 gives the details of the used grid.

Velocity inlet and pressure outlet boundary conditions are applied at the inlet and at the outlet, respectively (Figure 4). A sliding mesh technique is applied to the interfaces (impeller-volute interfaces 1 and 2 in Figure 4) in order to allow the unsteady interactions between the impeller and the volute. Turbulence is modeled with the  $k-\omega$  shear stress transport (SST) model. The governing equations are solved using the segregated solver and a centred SIMPLE algorithm is used for the pressure-velocity coupling.

### 3.2. Global characteristics

Simulations were carried out at flow rates  $0.5 q_{\text{bep}}$ ,  $0.8 q_{\text{bep}}$ ,  $q_{\text{bep}}$ , and  $1.2 q_{\text{bep}}$ . Figure 7 shows the pump head against flow rate for the two different pumps and their comparison with experimental data, as well as the predicted mechanical efficiency defined as  $\eta_m = q_v \Delta P / C_m$  with  $q_v$  the flow rate,  $\Delta P$  the static pressure, and  $C_m$  the moment.

In agreement with previous works [10] which express the slip factor as a growing function of the blade number, the numerical and experimental results of this paper confirm this fact: the splitted impeller head is approximately 10–15% higher than the original impeller whatever the flow rate is. The study of the flow morphology will show in Sections 3.3.1 and 3.3.2 that the splitter blades improve the flow conduction into the impeller and avoid the slow velocity zone at the blade pressure side. As a consequence, the average discharge angle  $\beta_2$  in the interblade channel is increased, improving the energy transfer to the fluid [11].

Concerning the efficiency, it appears that it is similar for the two pumps except at  $q_{\text{bep}}$  and  $1.2 q_{\text{bep}}$  where the original impeller presents a higher level. The lower efficiency of the impeller with splitters is a consequence of viscous loss on the additional blade surface.

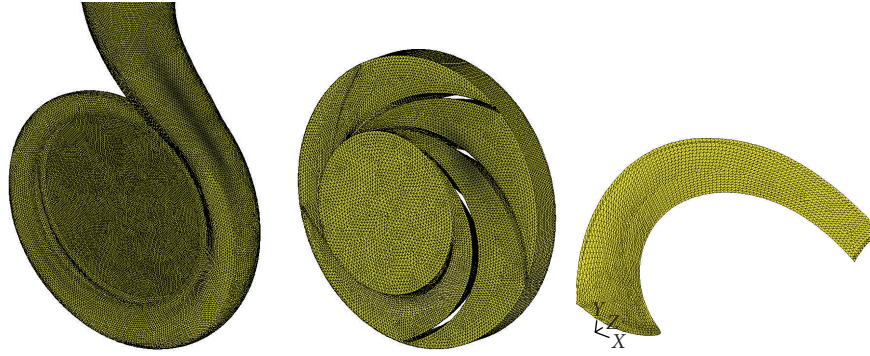


FIGURE 6: Meshes of the volute and impeller flow domains and triangular mesh on an isolated blade surface.

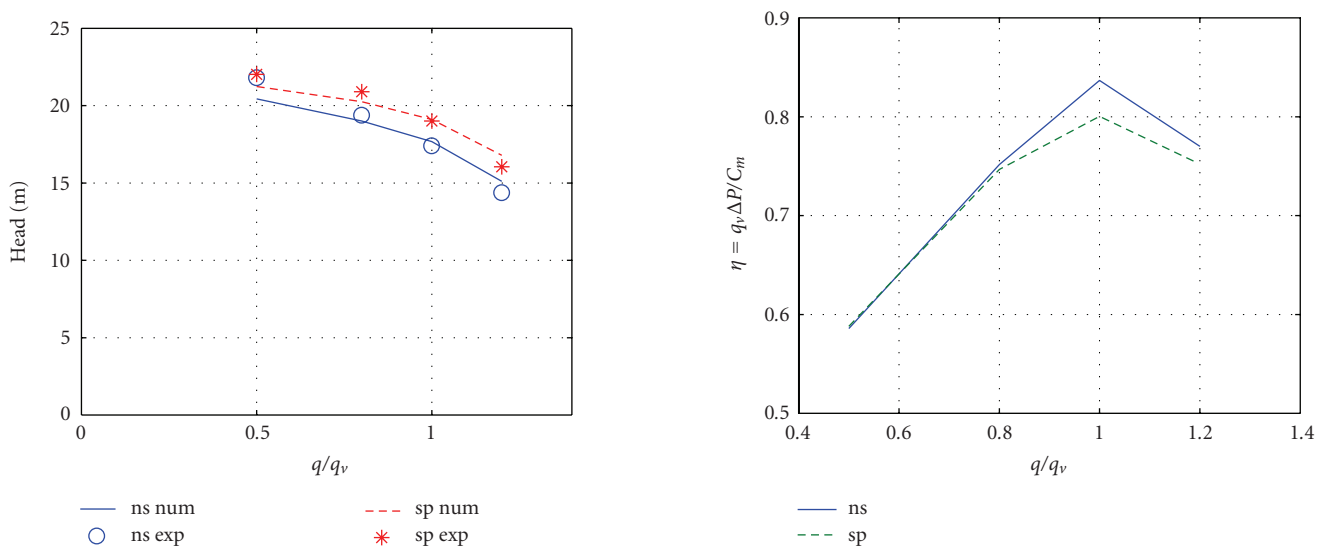


FIGURE 7: Head against flow rate ( $0.5 q_{bep}$ ,  $0.8 q_{bep}$ ,  $q_{bep}$ , and  $1.2 q_{bep}$ ),  $N = 900$  rpm, (a) comparison with test; (b) mechanical efficiency. ns = nonsplitted, sp = splitted.

### 3.3. Local characteristics

The flow in a centrifugal pump is highly three-dimensional and unsteady. The volute-impeller interaction can be described by two effects. The first effect, due to the axial asymmetry of the volute and the tongue presence, generates a nonuniform pressure distribution at the impeller outlet which is studied in Section 3.3.1. The second effect, owing to the flow impact leaving the channel against the tongue, causes pulsations that produce dynamical forces added to the previous ones. Section 3.3.2 deals with the complex velocity fields observed inside the pump.

#### 3.3.1. Pressure fields

Figure 8 shows the instantaneous static pressure distribution in the middle surface at  $q_v = 0.8 q_{bep}$ ,  $q_v = q_{bep}$ , and  $q_v = 1.2 q_{bep}$  for the original and splitted impellers. The conversion

of dynamic pressure produced by the impeller rotation into static pressure by the volute casing can be seen, thus the maximum of pressure is obtained in the outlet duct (except at high flow rate and at BEP for the splitted impeller).

Whatever the flow rate and the pump are, a nonhomogeneous pressure distribution is observed at the zone around the gap between volute tongue and impeller periphery, characterized by a high gradient of pressure. The volute tongue whose role is to drive the flow towards the fan outlet presents a singularity for the flow. The logarithmic shape of the volute casing creates a geometrical asymmetry, this phenomenon influences the pressure field distribution and fluctuating efforts applied on the impeller blades. At  $q_v = 0.8 q_{bep}$  and  $q_v = q_{bep}$ , the blade passage of the original impeller arriving at the volute tongue undergoes a strong pressure drop, so that a nonuniform pressure zone is created at the outlet section (see Figure 9). At  $q_v = 1.2 q_{bep}$ , the blade passage leaving the volute tongue experiences the largest pressure gradient.

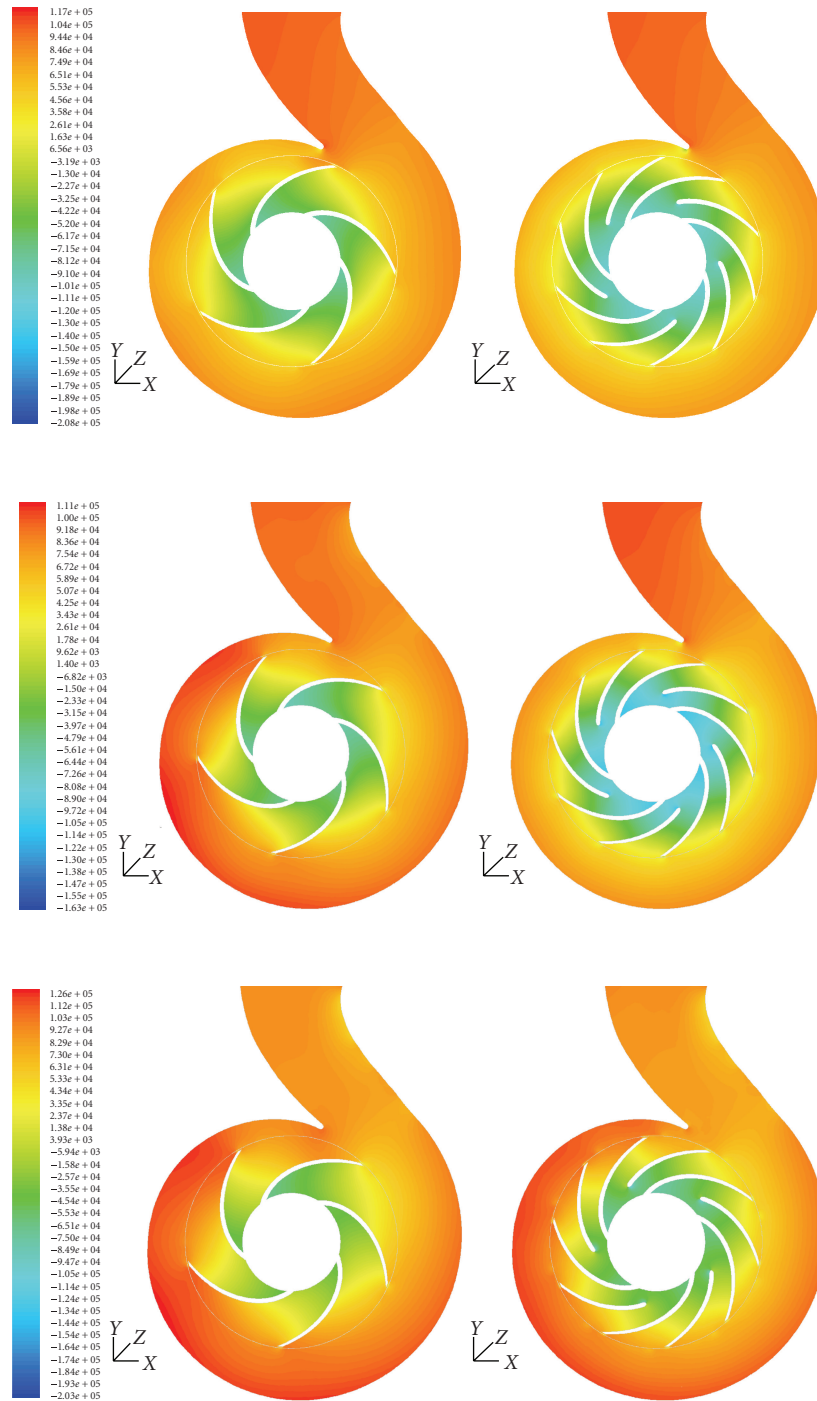


FIGURE 8: Computed static pressure fields at 80% (top), 100% (center), and 120% (bottom) of BEP at mean plane ( $z = 0$ ) for original (left) and splitted (right) pumps.

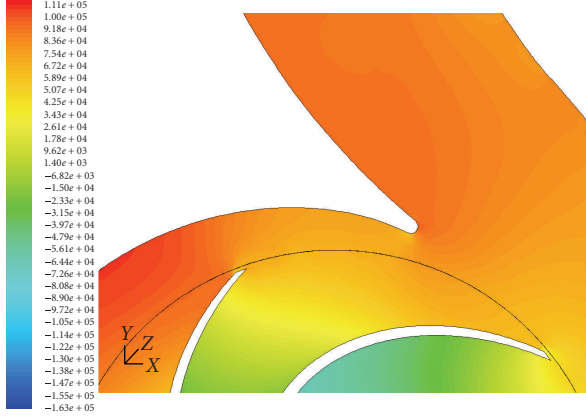
Its influence on the pressure field is stronger in the original pump than in the splitted impeller. However, at  $q_v = 1.2 q_{\text{bep}}$  the splitted impeller conducted the flow in a better way in the volute diffuser.

### 3.3.2. Velocity fields

The instantaneous velocity vectors in the pump are plotted in Figure 10 for the original and splitted impellers. The volute

TABLE 2: Mesh characteristics.

Fluid volume	Surf. mesh	Solid mesh	Size	Number of cells
Impeller	Tri.	Hybrid	2 (surf), 5 (solid)	600 000
Volute casing	Tri.	Hybrid	5	665 000
Upstream extent	—	Hex.(Cooper)	5	118 000
Downstream extent	—	Hybrid	10	153 000
			Total	1 535 000

FIGURE 9: Zoom on the volute tongue zone at  $q_v = q_{bep}$  for the original pump—numerical static pressure distribution.

tongue zone presents a strong recirculation of the fluid particles at the gap between the volute tongue and the impeller periphery.

The velocity fields show more significant variations when the pump works off the best efficiency point. For the original impeller at  $q_v = q_{bep}$  and for the two pumps at  $q_v = 1.2 q_{bep}$ , a dead volume zone with low velocity magnitude is observed in quarter a periphery from the volute tongue on. The volute tongue is a singularity for the flow that creates a strong recirculation zone at the volute diverging outlet where the fluid particles are slowed down (see Figure 11). At  $q_v = 1.2 q_{bep}$ , the impeller with splitter blades drives the fluid better than the original impeller. The slow flow velocity zone inside the impeller is avoided, as already observed at BEP. At flow rate  $q_v = 0.8 q_{bep}$ , a nonuniform velocity distribution is observed inside the splitter interblade channel. In fact, one of the splitter channels (at suction blade side) discharges a higher flow rate than the other.

Velocities are more homogeneous at the impeller periphery for the splitted pump. In fact, what occurs in the blade-to-blade space for the original pump is moved to the periphery of the impeller so that all the volute casing space is used.

### 3.4. Radial thrust

The nonuniform pressure distribution around the impeller periphery is the origin of periodic loads named the radial

thrust. An unbalanced radial thrust creates higher vibration amplitudes of the machine and affects the life cycle of the pump shaft and bearings. The pressure distributions around the impeller periphery which have been computed at different flow rates are plotted in Figure 12. The asymmetrical flow distribution can be observed, which confirms the computation results of Section 3.3 and in particular the presence of a nonzero radial thrust.

Since the impeller position compared to the volute tongue changes according to the case (it corresponds to the time step when the convergence has been reached), the pressure fluctuations are not synchronous to each other. It is anyway observed that the volute tongue corresponds to the zone which has the greatest influence on the global shape of the static pressure. In this zone, the static pressure takes almost the same value whatever the flow rate: around  $8.10^4$  Pa for the original pump and around  $7.10^4$  Pa for the splitted pump. Off this angular position, below the BEP ( $0.5 q_{bep}$  and  $0.8 q_{bep}$ ), the static pressure for the two pumps follows a decreasing slope except at the volute tongue where it meets a positive jump. At  $1.2 q_{bep}$ , the static pressure increases after meeting a negative jump in the volute tongue region. As expected, the weakest pressure pulsation amplitudes are found at BEP.

The radial thrust can be determined from the pressure distribution by carrying out the integration of the elementary forces around the impeller periphery (See Figure 13)

$$F = \sqrt{F_x^2 + F_y^2},$$

$$F_x = \int_0^{2\pi} dF_x(\theta) d\theta \quad \text{with } dF_x(\theta) = p(\theta) \cdot dS \cdot \cos(\theta),$$

$$F_y = \int_0^{2\pi} dF_y(\theta) d\theta \quad \text{with } dF_y(\theta) = p(\theta) \cdot dS \cdot \sin(\theta). \quad (1)$$

Figure 14 shows the amplitudes of the radial thrust against the pump flow rate for the two pumps. As expected, these curves reach a minimum at the BEP but it is surprising that the original pump presents a lower radial thrust than the splitted one. The radial thrust is particularly lower at the BEP where a 40% difference is observed. This is mainly due to the bigger interaction between the volute tongue and the flow for the splitted impeller: Figure 12 has indeed indicated a

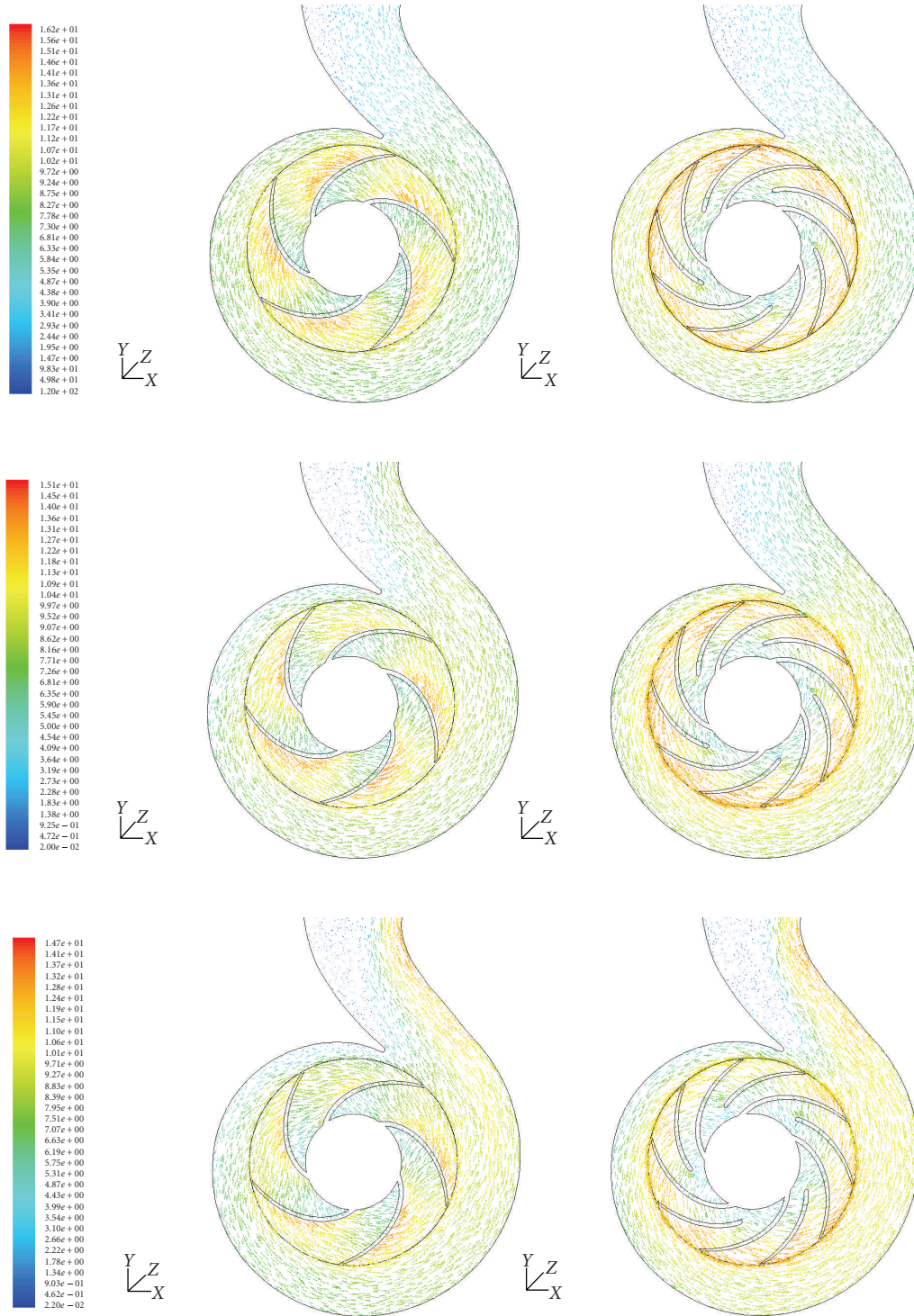


FIGURE 10: Computed velocity fields at 80% (top), 100% (center), and 120% (bottom) of BEP at mean plane ( $z = 0$ ) for original (left) and splitted (right) pumps.

more significant jump at the volute tongue position for this pump whatever the flow rate. By way of consequence the hydraulic unbalance is increased when adding splitters to the original impeller.

#### 4. TEST-ANALYSIS CORRELATION

Sensors are placed at the pump front flask and around the volute wall so that the influence of the distance can be observed.

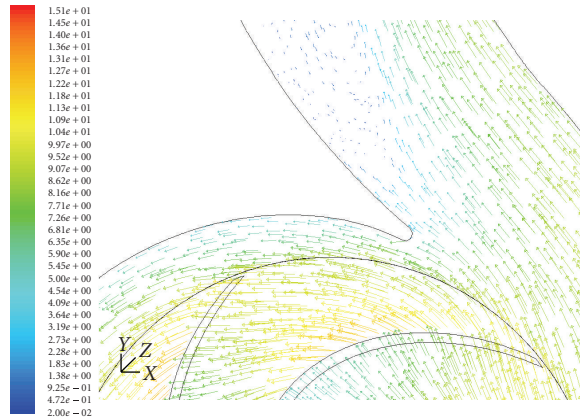


FIGURE 11: Zoom on the volute tongue zone at  $q_v = q_{bep}$  for the original pump—numerical velocity field prediction.

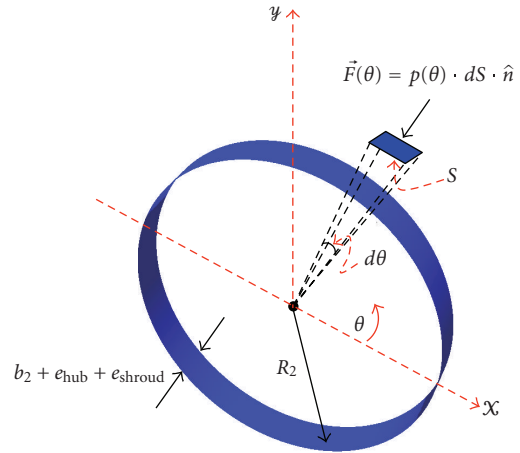


FIGURE 13: Radial force integration around the impeller periphery.

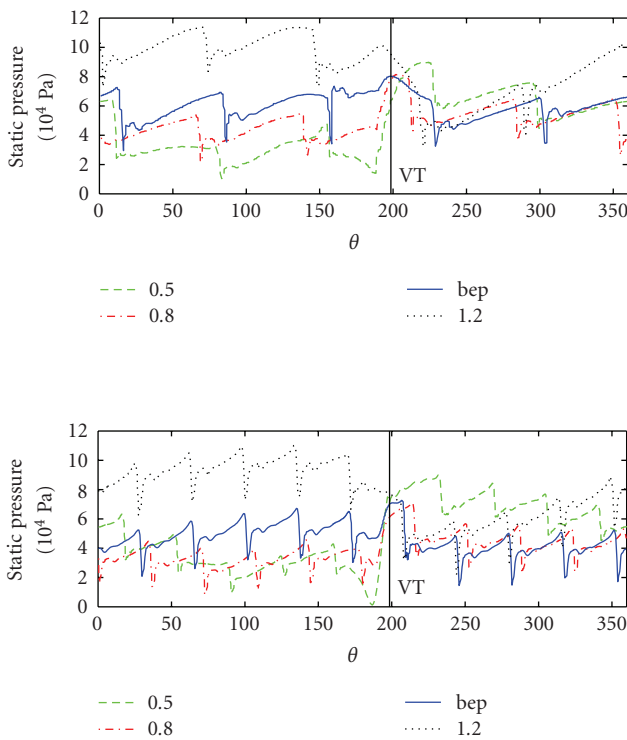


FIGURE 12: Static pressure distribution at the original (top) and splitted (bottom) impeller periphery at  $z = 0$  at  $0.5 q_{bep}$ ,  $0.8 q_{bep}$ ,  $q_{bep}$ , and  $1.2 q_{bep}$ . VT = volute tongue angular position.

A dynamic calibration of the sensors has been performed so that the measurement error can be quantified according to the frequency range. A spectral analysis has also been done to visualize the effect of the hydraulic unbalance of the pumping machine.

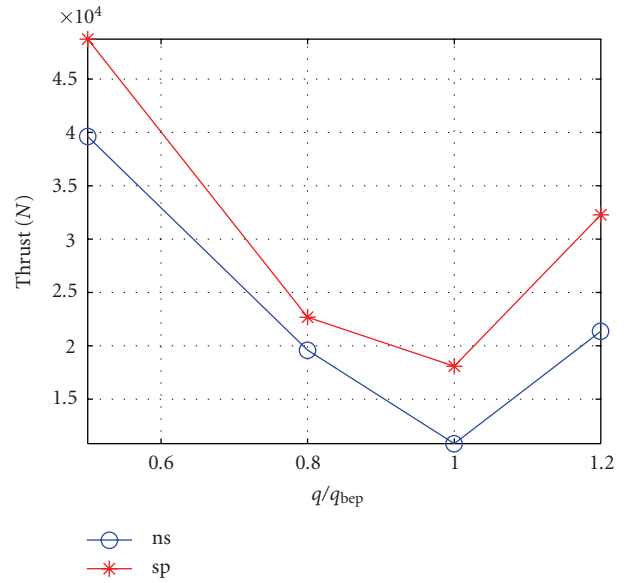


FIGURE 14: Amplitude of the radial thrust at different flow rates.

#### 4.1. Experimental setup

Measurements have been done using a spectrum analyzer Lecroy Type 9304A connected to a computer. To get the blade-to-blade pressure variations, four dynamic pressure outputs are measured using piezoelectric pressure sensors KISTLER 5011A which are glued to the volute flask, the wall of the volute casing, and the outlet duct. A selector switch allows to choose between these four sensors. The sensors are placed according to Figure 15 and their position is summarized in Table 3. One sensor is located at the pump front flask (Cp4). Two more sensors are located on the wall of the volute casing (Cp1, Cp2) and one more sensor is located on the outlet duct (Cp3).

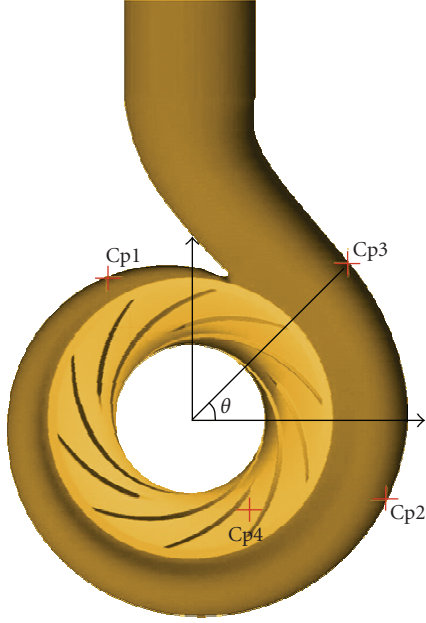


FIGURE 15: Kistler sensors locations for blade-to-blade measurements.

#### 4.2. Measurement uncertainty

The relation between the pressure at the transducer input and the measured voltage at its output can be modeled as

$$\Delta P = S * \Delta V + p_0, \quad (2)$$

where  $\Delta P$  is the pressure gap to which the pressure sensor is set,  $S$  its sensitivity,  $\Delta V$  the measured voltage, and  $p_0$  the atmospheric pressure. Equation (2) is defined in static but can be extended to quasistatic or dynamic measurements.

The pressure transducers are dynamically calibrated by applying a pressure test signal to the transducer input and by recording its output, in order to measure the drift of its sensitivity with frequency. The comparison of the obtained transfer functions with a reference transducer defines an uncertainty on the sensitivity  $S$ . The results on the frequency range 1–8000 Hz are obtained by means of three standardization devices (TCR and TC20 shock tubes and DOR20 quick open device [12]), under identical conditions of amplitude and frequency. The higher the frequency, the higher the uncertainty that never exceeds 12.5% (see Figure 16 and Table 4). This is quite acceptable for this study.

#### 4.3. Experimental spectral analysis

Figure 17(a) shows the presence of an additional signal of period  $f_N = N/60$  Hz which modulates the pressure fluctuations experimental measurements. This periodic signal which has the same frequency as the impeller rotation is identified as the hydraulic unbalance: it occurs when the

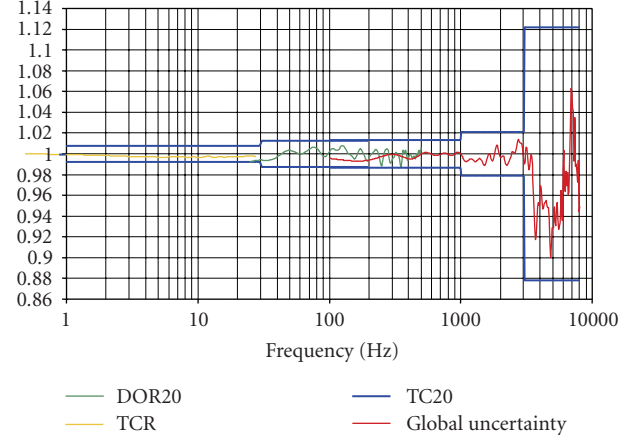


FIGURE 16: Measurement uncertainty against frequency.

TABLE 3: Sensor positions.

Sensor	Radius (mm)	$\theta(^{\circ})$
Cp1	On volute	120
Cp2	On volute	337
Cp3	On volute	60
Cp4	168	303

TABLE 4: Sensors calibration.

Frequency band	Uncertainty
1 Hz to 30 Hz	1.0%
31 Hz to 1000 Hz	1.5%
1001 Hz to 3000 Hz	2.5%
3001 Hz to 8000 Hz	12.5%

impeller gravity center in the water is off the rotation center and acts as an unbalance which modulates the pressure fluctuations with a periodic signal of frequency  $f_N$ . It then leads the signal fluctuations to be higher.

A Fourier analysis shows the hydraulic unbalance frequency at  $f_N$  whose level is as important as the blades frequency ( $5 f_N$  and  $10 f_N$ ) for sensor Cp3 (see Figure 17(b)). The farther one puts the sensor at the outstream duct, the bigger this perturbation is observed.

In order to compare them with the numerical results, the hydraulic unbalance has been removed from all the experimental data that are presented in this study using signal processing tools: in the frequency domain, after performing a fast Fourier transform, a filter centered at the frequency  $f_N$  has been applied to the signal. Since one aims at comparing the influence of splitters on the signals, one gets the insurance that the pressure fluctuations are only due to the blade passage.

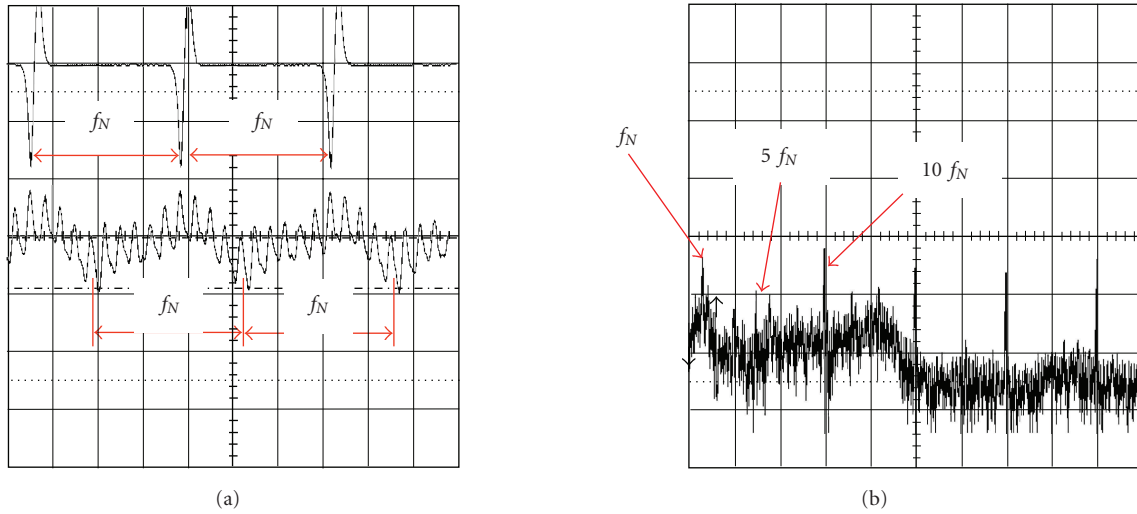


FIGURE 17: (a) Pressure fluctuations over three-time periods; (b) associated power spectrum—sensor Cp3 of splitted pump at BEP.

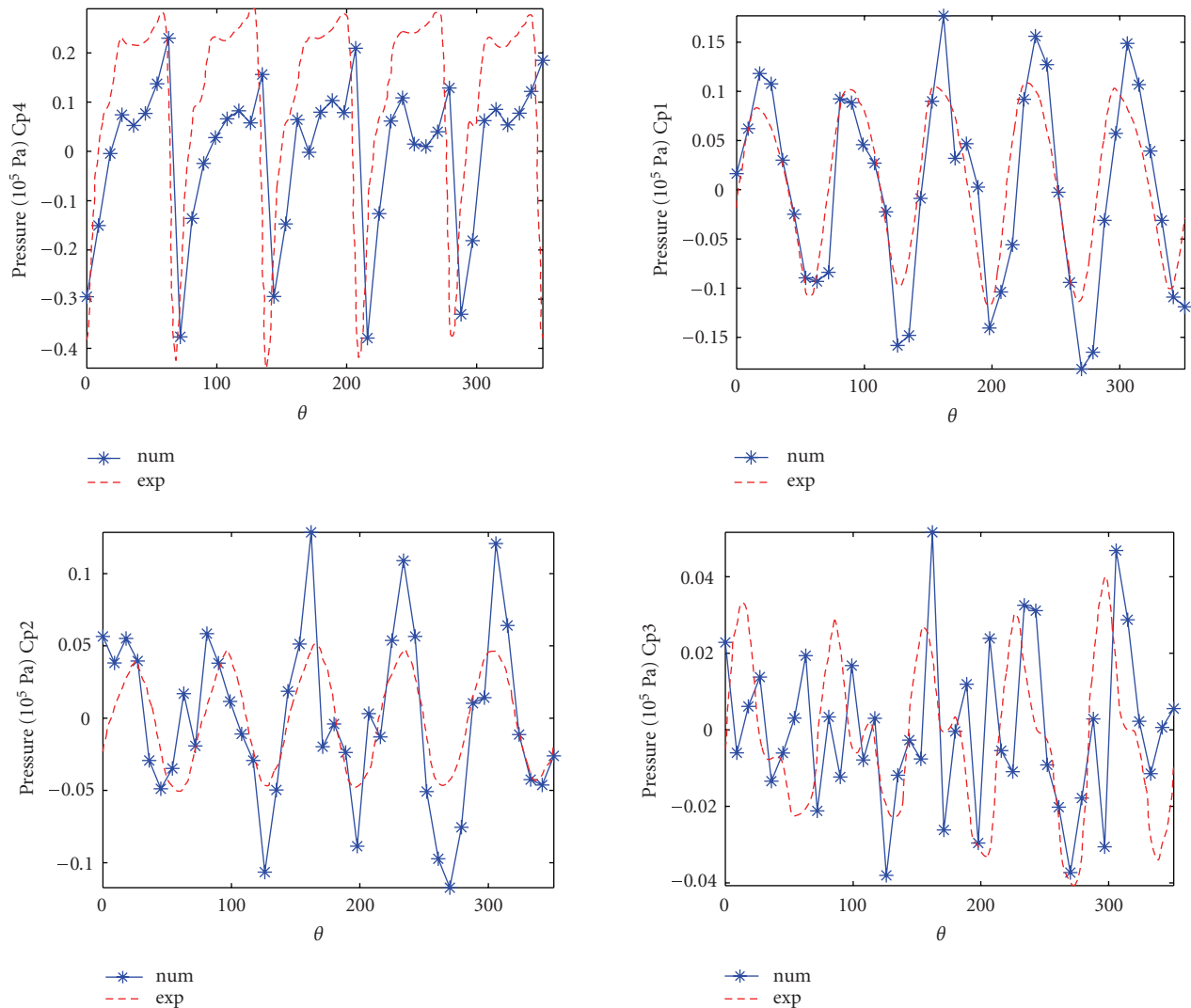


FIGURE 18: Computed and experimental pressure fluctuations over one impeller revolution—original impeller—sensors Cp4, Cp1, Cp2, and Cp3 at BEP; num = numerical, exp = experimental.

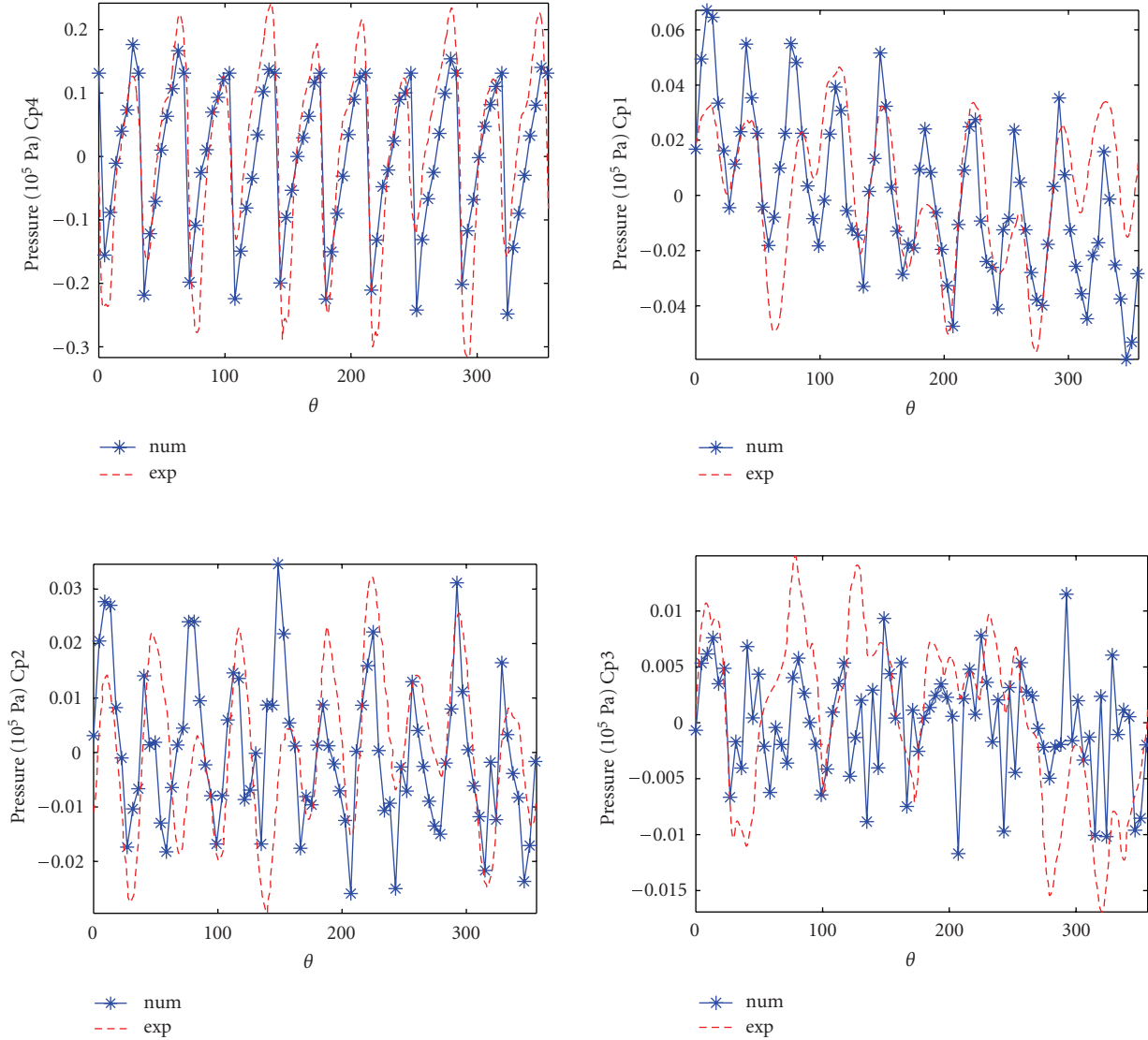


FIGURE 19: Computed and experimental pressure fluctuations over one impeller revolution—splittered impeller—sensors Cp4, Cp1, Cp2, and Cp3 at BEP; num = numerical, exp = experimental.

**4.4. Pressure fluctuations comparison**

The measurements have been taken in noncavitating tests at design flow rate for both pumps. Figures 18 and 19 present the measurements and their comparison with the results of the CFD simulation for the two pumps.

The experimental signals and those resulting from simulations are practically periodic. The observation of the pressure fluctuations over one period shows the passage of the 5 blades for the original impeller and 10 blades for the splitter blades model. The functional gap between the impeller and the volute flask has been taken into account in the simulation so that the signal levels agree.

A good agreement between the dynamical shapes of simulation and experimental results is reached for sensors Cp4

(on the pump front flask) and Cp1 (on the volute near the tongue) for the two pumps. The result remains approximate for sensors Cp2 and Cp3 where the numerical amplitudes are overestimated, except for sensor Cp3 for the splittered pump. This sensor is located at the outlet near the canal duct where experimental data are more difficult to get because of the flow perturbations (boundary layer instability) accompanied with a weaker fluctuation signal level.

A slight phase shift between the experimental and numerical signals is observed at the 4 locations for the original impeller (Figure 18): the experimental signal seems to be slightly in advance compared to the numerical one for sensors Cp4 and Cp1, then in accordance for sensor Cp2 and rather late for sensor Cp3. This is due to the nonuniform repartition of the blades on the impeller accompanied with a

TABLE 5: Pressure fluctuations level ratio between original and splintered pumps.

Sensor	$\Delta P$ original ( $10^5$ Pa)	$\Delta P$ splintered ( $10^5$ Pa)	Ratio
Cp4	0.61	0.43	1.4
Cp1	0.23	0.12	1.9
Cp2	0.11	0.06	1.9
Cp3	0.09	0.03	3

variable blade thickness, consequence of the impeller moulding. The numerical model does not take into account these small geometrical defects. On the other hand, Figure 19 does not present such a phase shift since the splintered impeller has been realized using a much more precise manufacturing process, which consists in milling the impeller according to the CAD model.

These results are full of information concerning the comparison of the pressure fluctuation levels. Adding splitters decrease the pressure fluctuations measured at sensors Cp4, Cp1, Cp2, and Cp3 by a factor from 1.4 to 3 (see Table 5 which precises the ratio for each sensor). This confirms the positive influence of adding splitter blades to the impeller in the objective to decrease the pressure fluctuations inside the volute and in the outstream duct.

## 5. CONCLUSION

The influence of splitter blades on the velocity and pressure fields in a centrifugal impeller (ENSIVAL-MORET MP 250.200.400 pump) has been analyzed by means of 3D simulations. A good agreement between global and local experimental and predicted results was found for a range of flow rates in this classical machine provided with the original impeller and a splintered one.

Adding splitters has negative and positive effects on the pump behavior. It increases the head rise compared to the original impeller; this is mainly due to the increase of the impeller slip factor which helps conduction of the flow. But the efficiency is not improved since the hydrodynamic losses are greater. It decreases the pressure fluctuations and reorganize more conveniently the flow at the volute outlet. But for all the studied flow rates it increases the interaction between the volute tongue and the flow. The consequence is an increase of the radial thrust.

The most important result is the minimization of the pressure fluctuations in order to decrease the vibrating acceleration level and radiated noise (class A pump: the fluctuations represent less than 2.5% of the static pressure). At the outlet duct (sensor cp3), it is improved by a factor 3.

Experimentally, one should measure with a manometer ring and control the vibrations using an accelerometer to see the positive influence of adding splitter on the vibratory behavior at the pump outlet duct.

## NOMENCLATURE

### Parameter

$R$	Radius (mm)
$b$	Impeller width (mm)
$\beta$	Blade angle ( $^\circ$ )
$\theta$	Blade inclination angle ( $^\circ$ )
$N_a$	Blade number
$e$	Blade thickness (mm)
$\Phi$	Diameter (mm)

### Subscript

0	Inlet
1	Inlet impeller
2	Outlet
3	Outlet volute
outlet	Outlet

## REFERENCES

- [1] H. PaBruker and R. A. Van den Braembussche, "Inverse design of centrifugal impellers by simultaneous modification of blade shape and meridional contour," in *Proceedings of the 45th ASME International Gas Turbine & Aeroengine Congress*, Munich, Germany, May 2000.
- [2] C. Cravero, "A design methodology for radial turbomachinery. Application to turbines and compressors," in *Proceedings of the ASME Fluids Engineering Division Summer Meeting (FEDSM '02)*, Montreal, Quebec, Canada, July 2001, paper FEDSM2002 - 31335.
- [3] D. Sloteman, A. Saad, and P. Cooper, "Designing custom pump hydraulics using traditional methods," in *Proceedings of the ASME Fluids Engineering Division Summer Meeting (FEDSM '01)*, New Orleans, La, USA, May-June 2001, paper FEDSM2001 - 18067.
- [4] A. Goto, M. Nohmi, T. Sakurai, and Y. Sogawa, "Hydrodynamic design system for pumps based on 3-D CAD, CFD, and inverse design method," *Journal of Fluids Engineering*, vol. 124, no. 2, pp. 329–335, 2002.
- [5] M. Asuaje, F. Bakir, S. Kouidri, R. Noguera, and R. Rey, "Validation d'une démarche de dimensionnement optimisé des roues centrifuges 2D par comparaison avec les outils de la simulation numérique (CFD)," in *10ème Conférence Annuelle de la Société Canadienne de la CFD*, pp. 560–565, June 2002.
- [6] D. Japikse, W. D. Marcher, and R. B. Furst, *Centrifugal Pump Design and Performance*, Concepts ETI, White River Junction, Vt, USA, 1997.
- [7] H.-W. D. Chiang and S. Fleeter, "Flutter control of incompressible flow turbomachine blade rows by splitter blades," *Journal de Physique. III*, vol. 4, no. 4, pp. 783–804, 1994.
- [8] C. Fradin, "Detailed measurements of the flow field in vaneless and vaned diffusers of centrifugal compressors," *Journal de Physique. III*, vol. 2, no. 9, pp. 1787–1804, 1992.
- [9] FLUENT. *Copyright 2005 Fluent*, 2005.
- [10] M. Asuaje, F. Bakir, S. Kouidri, T. Belamri, and R. Rey, "Modelisation of the slip factor of centrifugal pumps using the unsteady theoretical head computation," in *Proceedings*

*of the ASME Fluids Engineering Division Summer Meeting (FEDSM '01)*, New Orleans, La, USA, May-June 2001, FEDSM2001-18164.

- [11] F. J. Weisner, "A review of slip factors for centrifugal impeller," *Journal of Engineering for Power*, vol. 89, pp. 558–576, 1967.
- [12] Alessandro Borges de Sousa Oliveira, "Contribution à l'étalonnage dynamique des capteurs de pression - modélisation de l'estimation de l'incertitude associée," *Thèse ENSAM*, 2004.



# Hindawi

Submit your manuscripts at  
<http://www.hindawi.com>

